Development of oxidation models for space debris demise

P. Jorge[1], D. Henneaux[2], A. Turchi[3], T. Magin[4]

Abstract

During space debris atmospheric reentry, one of the important physical phenomena arising for metallic components is the formation of an oxide layer on the surface exposed to the high-enthalpy flow. Due to the change in material properties, the debris thermal behavior will be modified, e.g. the changes in emissivity and conductivity will affect the heat transfer by radiation and conduction, respectively. This work presents numerical tools developed to quantify and evaluate the importance of oxidation on the heat transfer mechanisms of reentering metallic debris. To achieve this, the oxide mass and thickness gains of Invar-36 oxidized in air plasma are numerically simulated in a 1-D finite difference framework. Moreover, a fully coupled mass-heat equation system is implemented allowing investigations of the thermal behavior of reentering oxidizing materials. The analysis is focused both on the surface effects of oxidation (emissivity change, heat of oxidation reactions) and in-depth effects caused by the changes in material properties (thermal diffusivity). CFD simulations are performed to retrieve the Stanton number and obtain explicitly the convective heat flux-wall temperature dependency. The influence of oxidation on the debris temperature is studied with six test cases representing full oxidation modelling, modelling of the emissivity changes, and no oxidation modeling at different flow conditions. Based on this analysis, neglecting oxidation induces an over-prediction of the material ablation and that in-depth modeling is necessary depending on the particular boundary conditions of the problem.

Keywords: *Space debris, Gas surface interaction, Oxidation modeling*

Nomenclature

Latin
CFD – Computational Fluid Dynamics
q – Heat flux
p – Pressure
T – Temperature
Greek
λ – Conductivity
Superscripts

conv – Convective
chem – Chemical
rad – Radiative
cond – Conductive

Subscripts

w – Wall
f – Fusion

1. Introduction

Due to the problematic size of the growing space debris population, space debris mitigation guidelines have been established to enforce a new design paradigm that ensures complete spacecraft disposal once the spacecraft end of life is reached. This can be accomplished by guaranteeing that when the spacecraft reenters the Earth's atmosphere, the extreme temperatures and heat fluxes caused by its hypersonic velocity will deteriorate the spacecraft structure and completely destroy it before reaching the ground.

The design of spacecraft following this new paradigm implies knowledge of the physical phenomena taking place during reentry. Space debris metallic materials are mostly composed of alloys whose main

[1] *von Karman Institute for Fluid Dynamics, Sint-Genesius-Rode, Belgium, pedro.jorge@vki.ac.be*

[2] *von Karman Institute for Fluid Dynamics, Sint-Genesius-Rode, Belgium, david.henneaux@vki.ac.be*

[3] *von Karman Institute for Fluid Dynamics, Sint-Genesius-Rode, Belgium, alessandro.turchi@vki.ac.be*

[4] *von Karman Institute for Fluid Dynamics, Sint-Genesius-Rode, Belgium, thierry.magin@vki.ac.be*

demise mechanism is the melting and, possibly, evaporation under the temperatures experienced during atmospheric reentry. This results in the presence of three phases (solid, liquid, gas) being the growth of the molten layer governed by the heat flux/temperature distribution and the balance of shear stresses and evaporation. No less important is the possible formation of an oxide layer on the surface of the debris as it may change important material properties such as the emissivity, melting temperature, conductivity, specific heat and density which, in turn, affects the heat transfer process inside the object. Although these effects can seriously alter the ablation rates, there is presently a lack of physical models and experimental results relevant for the problem of oxidation under reentry conditions.

The effect of dissociated oxygen on oxidation kinetics has been studied experimentally [1]. The effect of increased emissivity on the heat lost by radiation has been studied [2] using experimental procedures to quantify emissivity change with temperature and a flow environment that is relevant to the reentry problem. Furthermore, numerical simulations have been performed to evaluate the oxidation effect on the equilibrium temperature. However, the effect of conductivity and thermal diffusivity differences between oxide and alloy phases, as well as the effect of chemical fluxes due to oxidation on the overall object heat transfer are still an open question. To evaluate these effects, the solution of the coupled heat and mass transfer problem on the fine scale of the oxide layer is required.

The aim of the present work is to quantify the influence of oxidation on the thermal behavior of reentering metallic debris based on detailed material and hypersonic CFD simulations. For this purpose we consider the reentry of an Invar-36 ($Fe_{64} - Ni_{36}$) sphere under different reentry conditions. The material response code is implemented using finite differences and accounts for oxide layer growth by imposition of experimentally obtained growth kinetics. Moreover, the material property dependencies on temperature and composition are taken into account by using a solid-matter thermodynamic library. The flow and material codes are weakly coupled using the Stanton number approach in order to isolate flow and material effects without adding the complexity and the computational costs of a strong coupling.

2. Physical Modeling

This section describes present the physical models used to describe the oxide growth as well as the material thermal response to reentry.

2.1. Oxide growth Modeling

Oxidation results from the reaction of oxygen with the debris metal. After the initial stages of oxide formation, a thin film of oxide layer is formed which prevents direct interaction between the metal and the gas atoms. For the oxide layer growth to continue, transport of ions through the oxide lattice, from either the metal side or the surrounding environment air, has to take place.

Computational models for oxide growth that evaluate the concentration profiles in the metal phase are based on a multi-component diffusion problem that can be solved by considering Fick's second law. In this work we implement the model of Nijdam et al. to estimate the change in alloy composition with oxidation[3]. Taking the solvent as the alloy element M^{III}, a three element diffusion problem reduces to a system of two partial differential equations of the form:

$$\frac{\partial C_a}{\partial t} = \frac{\partial}{\partial x}\left(\tilde{\mathcal{D}}^n_{aa}(C,T)\frac{\partial C_a}{\partial x} \right) + \frac{\partial}{\partial x}\left(\tilde{\mathcal{D}}^n_{ab}(C,T)\frac{\partial C_b}{\partial x} \right) \qquad a,b = M^I, M^{II}, \tag{1}$$

where C_a is the concentration of element a in the alloy (kg/m^3 or $moles/m^3$), M^I, M^{II} are the alloy elements. In order to close the equations, two boundary conditions are needed. The length of the domain with respect to the diffusion length scales allows considering a semi-infinite boundary condition on the face opposite to the oxidation front. Moreover, the growth of the oxide imposes an oxide/metal interface concentration to satisfy mass conservation. The boundary condition where oxide grows consists of 5 algebraic equations that link the imposed oxide growth rate with the availability of each alloy constituent to form oxide. The equations are detailed on the thermodynamic model of Nijdam [3]. The model considers the reaction of the alloy components with oxygen at pressure and temperature to form pure oxides ordered by their standard Gibbs free energy of formation per mole of oxygen. As an input, the

formulation requires the growth kinetics of the oxide layer, usually determined experimentally. The kinetics can be determined as mass/thickness gains versus either time or temperature [4].The model is able to compute the metal in-depth concentration profiles as well as the quantities of each oxide formed.

2.2. Material thermal response

The thermal response of the material is modeled for the alloy and oxide phase. The heat equation is considered in which the material properties are taken as dependent on temperature and composition making the equation non-linear. To close the heat equation, two boundary conditions need to be provided. The boundary not exposed to the flow is assumed to be an adiabatic or a radiating surface. The effects of these assumptions are analyzed in Section 5. At the boundary exposed to the flow, the balance equation has to account for convection from the surrounding flow, chemical heat fluxes, re-radiation and conduction to the bulk material q_w^{conv},q_w^{chem},q_w^{rad} and q_w^{cond}, respectively. The boundary condition in compact form is

$$q_w^{conv} + q_w^{chem} = q_w^{cond} + q_w^{rad}. \tag{2}$$

Each heat flux component is detailed hereafter.

Oxidation is an exothermic process so a contribution to the net heat flux is expected from this phenomenon. Assuming that all the heat of reaction is given up to the oxide phase and knowing the mass of each oxide formed the chemical heat flux can be computed as:

$$q_w^{chem} = \sum_{i=1}^{N_{ox}} H_{ox_i} \Gamma_i \tag{3}$$

where Γ_i is the amount of oxide i created and H_{ox_i} is the heat of reaction for the creation of oxide i. Care should be taken as the chemical flux is different for the reaction with atomic and molecular oxygen. Regarding radiation, it is well established that many metals and alloys used in space applications develop oxides with significantly higher emissivities than their parent alloys [4, 1]. The emissivity change will influence the heat lost by radiation given by the Stefan-Boltzmann law.

Contrary to emissivity, the conductivity of an oxide is usually much smaller than that of the parent alloy. Additionally, if the oxide scale is porous the conductivity can be even lower[5]. Conduction is modeled following Fourrier's law and the variation of conductivity with temperature and concentration is considered. For alloys, the thermal conductivity is composed of a contribution from heat transporting electrons predominant in metals, and another contribution from lattice waves/phonons predominant in ceramics [6]. The total thermal conductivity is given as the sum of these two excitations. In this work, both contributions are considered and modeled following the principles stated in [6].

The convective heat flux may be obtained from detailed CFD simulations or by analytical expressions. In this project CFD simulations are performed using the FVM code Cosmic [7]. The convective heat flux is also dependent on the surface temperature which would mean, if a similar formulation is used, that a coupling of the material and flow solvers should have been performed to evaluate the effect of oxidation on the surface temperature. A simpler solution consists in expressing the convective heat flux as function of a dimensionless heat transfer coefficient, the Stanton number as in[8]:

$$q_w^{conv} = \rho_e u_e C_h (h_{r,e} - h_w) \tag{4}$$

where the subscript e refers to the conditions at the boundary layer edge and $h_{r,e}$ is the recovery enthalpy. With the present formulation, for a specific flow condition, it is possible to obtain an expression for the convective heat flux that explicitly depends on the wall temperature.

3. Computational methodology

3.1. Oxide growth

The concentrations in the bulk of the alloy are computed with an Euler explicit finite difference scheme. Equation (1) is expressed in conservation form as a second order central finite difference approximation:

Table 1. Model input summary

Model	$\Delta G^0_{\mathrm{M^J}_x O_y}$	$V_{\mathrm{M^J}_x O_y}$	a_J	$\tilde{\mathcal{D}}^{Ni}_{ij}$	$\bar{V}_J$	Growth Kinetics
Nijdam [3]	[11]	[12]	Thermo-Calc	Not given	Not given	[3]
Present Work	[11]	[12]	Thermo-Calc	[13]	Thermo-Calc	[3]

$$C^{n+1}_{a,i} - C^n_{a,i} = \beta^{aa}_{i+\frac{1}{2}}(C^n_{a,i+1} - C^n_{a,i}) - \beta^{aa}_{i-\frac{1}{2}}(C^n_{a,i} - C^n_{a,i-1})$$
$$+ \beta^{ab}_{i+\frac{1}{2}}(C^n_{b,i+1} - C^n_{b,i}) - \beta^{ab}_{b,i-\frac{1}{2}}(C^n_{b,i} - C^n_{b,i-1}) \tag{5}$$

where a and b are the alloy elements as in Eq (1), $\beta^{aa}_{i+\frac{1}{2}} = \tilde{\mathcal{D}}^{aa}_{i+\frac{1}{2}}\frac{\Delta t}{\Delta x^2}$ is the Neumann number computed with the interdiffusion coefficient of element a interpolated between two nodes: $\tilde{\mathcal{D}}^{aa}_{i+\frac{1}{2}} = \frac{\tilde{\mathcal{D}}^{aa}_{i+1}+\tilde{\mathcal{D}}^{aa}_i}{2}$ for an equally spaced mesh with size $\Delta x = \sqrt{2D_0 t}$, taken to respect the stability constraint of the timee integration scheme. The thermodynamic library Thermo-Calc [9] was used to compute the interdiffusion coefficient depending on temperature and composition.

After the bulk concentrations are computed, the interface concentrations are the last missing element to obtain the full concentration profiles in the alloy. This entails testing different equilibrium concentrations and solving the 5 additional equations mentioned in Section 2.1. The lengthy full numerical procedure can be found in [3] and [10].

After the concentration profiles and all oxide thicknesses are computed for $t + \Delta t$, the mesh is misaligned since the interface oxide/metal interface has moved $\xi^{t+\Delta t}$. To keep the mesh conformed with the interface, the computational domain has to be adapted to maintain a constant grid spacing as:

$$\Delta x = \frac{x(L) - \xi^{t+\Delta t}}{L - 1} \tag{6}$$

where L is the number of grid points and $x(L)$ is the domain size, which is fixed. The concentrations at the new node positions are interpolated from the previous grid using a piecewise cubic hermite polynomial (PHCP).

3.1.1. *Validation of the oxide growth model*

The computational oxide growth model was applied to the oxidation of $Ni_{64}-Cr_{27}-Al_9$(at.%) at 1373K and oxygen partial pressure $p_{O_2} = 10 \times 10^4$ Pa. The aim is to validate the present model with the numerical and experimental work of [3]. The inputs were, as much as possible, the same as the ones in [3] and are summarized, for reference, in Table 1. More details are given in [10].

Figures 1(a) and (b) show the obtained concentrations profiles in the alloy plotted against the experimental and numerical results of [3]. From Fig. 1(a) it is clear that the profile obtained with the present model should be sharper when compared with the experimental data. This discrepancy is attributed to the overestimation of the diffusivity of aluminum in the material. Nonetheless, the interface concentration of aluminum is consistent with the experimental and numerical results. On the other hand, Fig. 1 (b) shows a good agreement between the experimental chromium curves and the numerical model of the present work. Additional details regarding the validation are presented in [10]

3.2. Material thermal response

To analyze the material thermal response, the heat equation is discretized and coupled with the mass balance Eq. (1). Applying the same spatial discretization as in Eq. (5) and dividing and multiplying by Δt one obtains, for the energy equation:

$$\frac{\partial e}{\partial t} = \lambda_{i+\frac{1}{2}}(T_{i+1} - T_i) - \lambda_{i-\frac{1}{2}}(T_i - T_{i-1}), \tag{7}$$
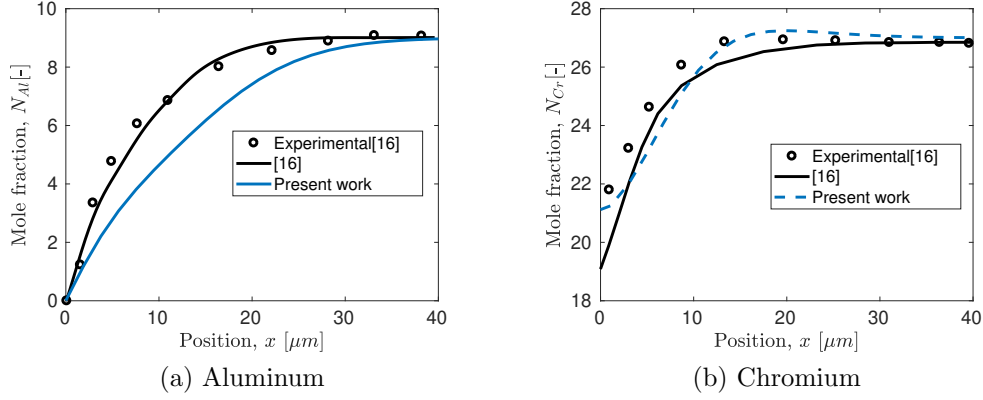
(a) Aluminum   (b) Chromium

Fig 1. Computed and experimental concentration profiles comparison for $t = 0.2\,\text{h}$ for the oxidation of $\text{Ni}_{64}-\text{Cr}_{27}-\text{Al}_9$ at $T = 1373\,\text{K}$, Data from [3]

where e is the energy density given as $e = \rho c_p T$ and $\lambda_{i+\frac{1}{2}}$ is the conductivity evaluated with an harmonic average between the two nodes i and $i+1$[14]: $\lambda_{i+\frac{1}{2}} = \frac{2\lambda_{i+1}\lambda_i}{\lambda_{i+1}+\lambda_i}$. Moreover, $\gamma_{i+\frac{1}{2}} = \frac{\lambda}{\rho c_p}\frac{\Delta t}{\Delta x^2}$, is the Neumann number for the temperature equation using the conductivity of the alloy. The Neumann number for the heat conduction equation is much larger than the Neumann number for the mass balance ($\gamma \gg \beta$) i.e., the conduction of heat is much faster than the diffusion of mass. For this reason it would be inappropriate to solve both equations explicitly. Hence, an Euler implicit scheme was used for the time discretization of Eq. (7) and the discretized equations are given as:

$$e_i^{n+1} - e_i^n = \frac{1}{2}\left(\lambda_{i+\frac{1}{2}}^{n+1}(T_{i+1}^{n+1} - T_i^{n+1}) - \lambda_{i-\frac{1}{2}}^{n+1}(T_i^{n+1} - T_{i-1}^{n+1})\right) \tag{8}$$

where the conductivity λ and specific heat, and therefore γ, are evaluated at the level $n + 1$. Note that, λ, c_p and ρ are dependent on temperature making the system of equations non-linear. Moreover the boundary condition given by Eq (2) is discretized as follows:

$$\rho_e u_e C_h(h_{r,e} - h_w) + \sum_{i=1}^{N_{ox}} H_{ox_i}\Gamma_i - \epsilon(T_w)\,\sigma T_w^4 - \lambda(T_w)\frac{T_w - T_2}{\Delta x} = 0 \tag{9}$$

where ρ_e, u_e, C_h, $h_{r,e}$ are constant for a given flow condition. Finally, the right boundary condition is considered as an adiabatic wall.

In order to couple the mass and energy equations, the same mesh is used for both equations. Since the mass equation is solved explicitly while the energy equation is solved implicitly the mesh sizing is fixed given a certain time-step as described in Section 3.1.

3.2.1. Sub-grid moving boundary treatment

The oxide growth in each time step is known and can be tracked, but, does not coincide with the adopted mesh spacing. For this reason, special care is taken to obtain meaningful material properties in the cells in which the oxide layer is growing by volume averaging the conductivity, specific heat and density in the cell. This way, one can obtain effective material properties by considering information of sub-grid phenomena as:

$$\phi_{eff} = \frac{(\xi - x_i)\phi_{ox} + (x_{i+1} - \xi)\phi_{alloy}}{h} \tag{10}$$

where ϕ represents the different material properties i.e., conductivity, specific heat and density. Numerically, Eq. (10) is used to update the interface node values present in Eq. (8) in the particular cell where the oxide is growing (see Fig. 2).
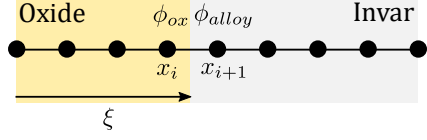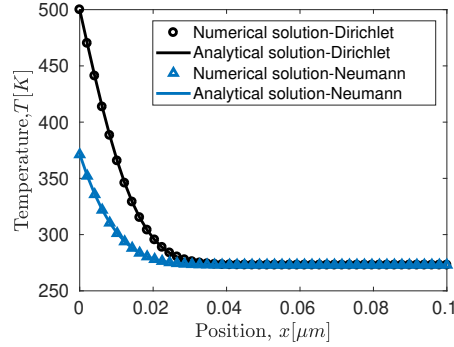
Fig 2. Schematic of sub-grid property averaging

Fig 3. Validation of constant coefficients heat equation with Dirichlet/Neumann conditions at $t = 600\,\text{s}$

3.2.2. Verification of heat equation

To verify the implementation of the heat equation, the analytical solutions of the heat equation[15] for a semi-infinite solid and imposed temperature/flux were implemented. Figure 3 shows a comparison of the analytical and numerical solution of the equation for the test case of heat conduction in a 1-D rod with thermal diffusivity $\alpha = 4.1 \times 10^{-12}$ m^{2}s^{-1} and surface and bulk temperature $T_s = 500\,\text{K}$, $T_b = 273\,\text{K}$, respectively. The analytical and numerical curves collapse to each other confirming the correct implementation of the numerical scheme.

4. Test case description

In this section we describe the set-up of the present test case dealing with the survivability of a sphere of Invar-36 ($\text{Fe}_{64} - \text{Ni}_{36}$). Invar-36 is approximated as a two component alloy and is a particular case of the three-component model detailed in the previous sections. This requires modeling the flowfield, the definition of the heat equation boundary condition inputs, (9), namely thermal diffusivity α, emissivity ϵ, wall fluid enthalpy h_w and heat of reaction H_{ox}. Moreover, the growth kinetics of the oxide also have to be defined.

4.1. Flowfield modeling

In order to obtain a relevant heat flux, the reentry conditions of a sphere, representative, for example, of a pressure vessel, was simulated using the CFD code Cosmic. Cosmic [7] is a 2-D/axi-symmetric Euler/Navier-Stokes code which includes the required physico-chemical models for high enthalpy re-entry flow modeling. To simulate reentry conditions, representative physical quantities at the inlet were chosen and are summarized in Table 2. Exploiting the symmetry of the problem only a quadrant of the sphere is simulated and a symmetry axis is considered on the stagnation line of the sphere. The wall is taken as a non-catalytic wall at 1400K.

Table 2. Test conditions for sphere.

p_∞(Pa)	T_∞(K)	M_∞	$Y[N2]_\infty$	$Y[O2]_\infty$	$Y[NO]_\infty$	$Y[N]_\infty$	$Y[O]_\infty$	T_{wall}(K)
1000	300	9	0.77	0.23	1e-20	1e-20	1e-20	1400

Before obtaining the results, a brief grid convergence study was performed. Three meshes were compared each with double the points of the previous. The stagnation point heat flux is compared for the three meshes and is observed to converge. More details of the grid convergence study can be obtained in [10].

Moreover, due the formulation of the Stanton number in Eq. (4), the position of the boundary layer edge needs to be found so that h, ρ and u are evaluated at the edge of the boundary layer. The boundary layer
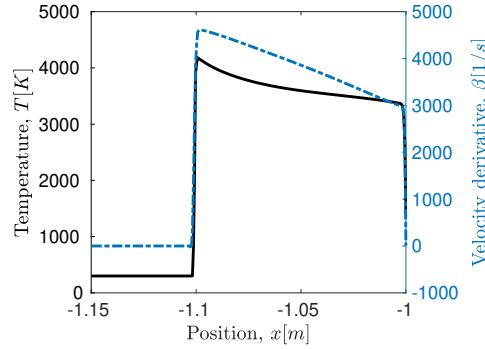
Fig 4. Temperature and β parameter vs position

is computed following the methodology stated in [16]. The method is to consider the boundary layer thickness as the point where the behavior of the velocity gradient $\beta = \frac{dv}{dy}$ stops being linear with regards to the x direction. Fig. 4 shows β at the stagnation line plotted along with temperature and it can be seen that the deviation from linear behavior occurs at a similar point for both quantities as stated in [16].

4.1.1. Oxide experimental growth rate

The experimental Invar plasma oxidation campaign of [4] provided the necessary oxide growth rate for the present work model. Firstly, to obtain the driving force for oxidation the mass gain vs time ($0\,\text{s} \leq t \leq 500\,\text{s}$) curves are obtained for specific temperatures. For example, at $T = 1650\,\text{K}$, the mass gain is given, as function of time, by a parabolic curve as

$$\frac{\Delta m}{S} = 14.227\sqrt{t}, \tag{11}$$

for the case of oxidation in air plasma at $300\,\text{Pa}$. The average mass gain rate for a specific temperature can be obtained dividing the total mass gain by the total oxidation time of the experiment. The experimental results yield two oxidation regimes for the evolution of mass gain rate versus temperature:

$$\begin{cases} \dfrac{\Delta m}{St} = 4.11\exp(\dfrac{-4828}{T}), & T \leq 1450\,\text{K} \\ \dfrac{\Delta m}{St} = 150000\exp(\dfrac{-19452}{T}), & T \geq 1450\,\text{K} \end{cases} \tag{12}$$

These relations allow obtaining an average growth rate that would be correct should the oxide growth kinetics be linear. However, the real kinetics of this test case are parabolic and using this average growth rates will lead to underestimation of the mass gain as it can be seen in Fig. 5. The following procedure was followed to avoid this underestimation. Firstly, it is possible to retrieve the initial parabolic curves from the average growth rates given in Eq. (12) if the total oxidation time is known. Moreover, theoretically, parabolic kinetics are only observed when the oxide film is already thick ($\approx 1\,\mu\text{m}$) [17]. For this reason, the growth kinetics are taken as linear until the oxide layer thickness reaches $1\,\mu\text{m}$. When this thickness is achieved, imposing continuity and continuous differentiability, a parabolic curve is fitted to respect the growth rate imposed by the average growth rate curves, as it can bee seen in Fig. 6. To march in time and obtain the mass growth in a time step one has to identify, in the growth curve at the updated temperature, the time which corresponds to the mass already gained. Subsequently, adding the timestep to the known time at this temperature will yield the total thickness after the new timestep and the mass gain can be easily calculated.

4.1.2. Emissivity estimation

To estimate emissivity, the experiments of [4] were post-processed. Figure 7 shows the dispersion graphs of the experimental results obtained in the MEDIASE facility [18]. Two linear regressions were performed
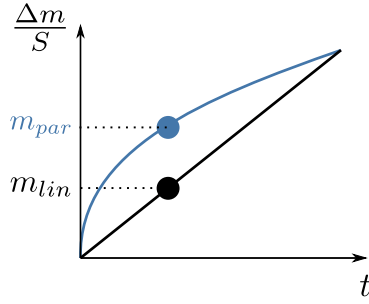
Fig 5. Mass gain as calculated with average growth rate (black) or actual growth kinetics (blue)
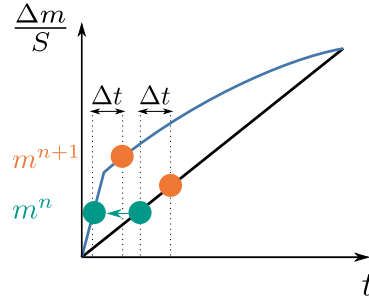

Fig 6. Schematic of time stepping procedure for mass growth and comparison with average growth rate assumption

on the experimental data, to fit the oxide and alloy emissivity measurements. The obtained regressions and correlation coefficients are:

$$\begin{cases} \epsilon_{ox}(T) = 1.058 - 2.82 \times 10^{-4}T, & R^2 = 0.4 \\ \epsilon_{Inv}(T) = 0.187 + 8.0913 \times 10^{-5}T, & R^2 = 0.208 \end{cases} \tag{13}$$

Although the fitness goodness is not completely satisfactory, this approximation should be sufficient to qualitatively evaluate the effects of emissivity increase due to oxidation.
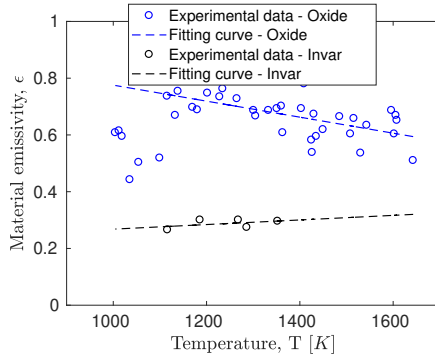
Fig 7. Emissivity measurements and fitting curves for Invar and Invar oxides
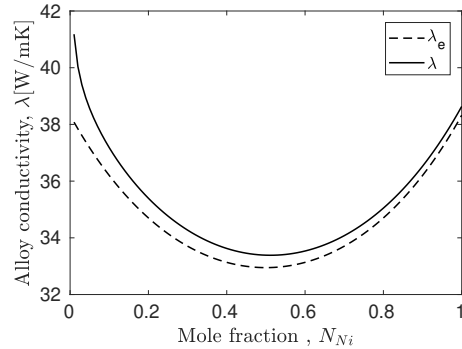
Fig 8. Electronic and total conductivity for Invar at $T = 1650\,\mathrm{K}$

4.1.3. Thermal diffusivity estimation

The values of conductivity for the metal and oxide have to be estimated to provide an approximation for the conduction term in the net heat flux balance as well as bulk properties. A wide range of values was found in the literature for the conductivity of hematite/magnetite[19, 20, 21] with $\lambda_{ox} \in [1-5]\frac{\mathrm{W}}{\mathrm{mK}}$ and no available values for the high temperatures reached during reentry. Both values in the range will be tested.

Figure 8 shows the values for the estimation of Invar thermal conductivity dependency on composition at $T = 1650\,\mathrm{K}$ based on the model presented in Section 3. The data for the conductivity of pure iron and the non-depleted conductivity of Invar were extrapolated from [6].

In order to obtain the alloy specific heat and density depending on temperature and composition the thermodynamic library Thermo-calc[9] was used. Fig. 9 and 10 show the specific heat and density for Invar36. The data for the oxide was obtained similarly and can be approximated to be constant with temperature.
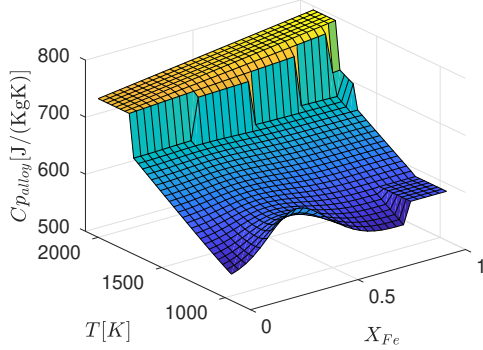
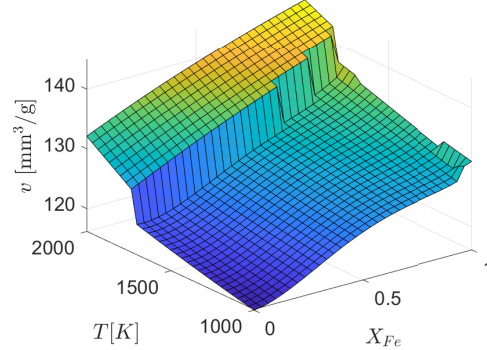**Fig 9.** Specific heat vs alloy composition and temperature for $Fe_{64}-Ni_{36}$, obtained with Thermo-Calc

Fig 10. Specific volume vs alloy composition and temperature for $Fe_{64}-Ni_{36}$, obtained with Thermo-Calc

4.1.4. Heat of reaction estimation

To compute the correct heat reaction we simplify the problem to consider the reaction of Invar with air plasma as the reaction of iron with molecular and atomic oxygen:

$$\begin{cases} 2Fe(s) + 3O(g) = Fe_2O_3, & H_1 \\ 2Fe(s) + \frac{3}{2}O_2(g) = Fe_2O_3, & H_2 \end{cases} \tag{14}$$
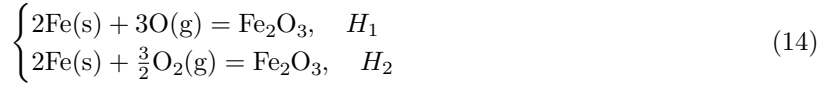
where H_1, H_2 are the heats of reaction for the oxidation with atomic and molecular oxygen, respectively. Moreover, H_1 is computed using Hess's law and the formation enthalpy of atomic oxygen. To compute an effective heat of reaction one considers the number flux of each species to the surface given by the Hertz-Knudsen equation:

$$\dot{m}_i = p_i \sqrt{\frac{1}{2\pi m_i k_B T_w}} \tag{15}$$

From flowfield simulations we obtain a dissociation rate of the plasma flow of 70% for the present case and compute the number flux of molecular and atomic oxygen impinging on the wall. If we consider no preferential oxidation by atomic or molecular oxygen and consider the stoichiometric coefficients for each reaction, the effective heat of reaction can be computed as:

$$H_{ox,eff} = 3\frac{\dot{m}_O}{\dot{m}_O + \dot{m}_{O_2}}H_1 + \frac{3}{2}\frac{\dot{m}_{O_2}}{\dot{m}_O + \dot{m}_{O_2}}H_2 \tag{16}$$

4.1.5. Near-wall fluid enthalpy estimation

To compute the near wall fluid enthalpy dependency on temperature, the "mppequil" tool in Mutation++[22] was used. This allows computing the enthalpy of air at equilibrium at a given temperature and pressure. Considering that the pressure is known from CFD simulations the wall enthalpy, h_w, will only be a function of temperature and is given as an output, in table form. From here, one has only to apply an interpolation function to obtain the temperature dependent convective term.

5. Results

In order to evaluate the influence of oxidation on the surface temperature and implicitly on the survivability of space debris, Invar-36 oxidation in air plasma is considered.
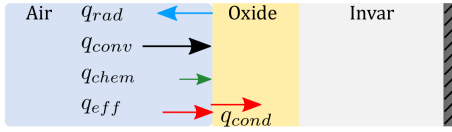
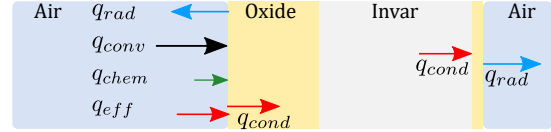**Fig 11.** Thin slab problem schematic and heat fluxes for a adiabatic posterior surface

Fig 12. Thin slab problem schematic and heat fluxes for a radiating posterior surface

5.1. Characterization of oxidation influence on demise

The simulation of a thin slab reentry is performed taking into account the numerical methodology presented in Section 3. The front of the material undergoes oxidation by influence of the incoming flow and on the posterior surface an adiabatic or radiating boundary condition is considered as shown in Fig. 11 and 12, respectively. The results are divided in two sections detailing adiabatic and radiating boundary conditions. In each section, simulations of different flow conditions, thicknesses as well as the three test cases are analyzed.

The mass and heat equation are coupled and the domain is comprised of two mesh blocks: one with 100 points and approximately $250\mu m$ of length is used to model oxidation and the oxide growth; the second mesh block starts at the end point of the first and extends the domain, following a geometric progression of constant 1.08, to approximately $3\,cm$ or $30\,cm$. In the second mesh block the conductivity and specific heat change only with temperature as concentration gradients due to oxidation are extremely local and are captured in the first mesh block. The simulations are started with an initial temperature of $1000\,K$ and no initial oxide layer.

The study methodology is to consider three modeling approaches: one where oxidation is modeled in depth and the oxide growth is modeled taking into account the changes in emissivity, conductivity, density and specific heat, this approach is referred to as "In-Depth"; one where oxidation is considered as a purely surface phenomena, being no in-depth oxide layer modeled, but accounting for the changes in emissivity and chemical heat flux resulting from oxide growth, this case as referred to as "Surface"; lastly, oxidation is disregarded completely and the properties are taken for the alloy, this approach is referred to as "Metal". To evaluate if melting is present, the fusion temperatures of both Invar($T_f = 1710\,K$) and hematite ($T_f = 1838\,K$) are prescribed.

5.1.1. Adiabatic posterior surface

Firstly, the case of posterior adiabatic surface is considered as shown in Fig. 11. For the flow condition of $C_h = 0.012$, obtained with the CFD simulations the fusion temperature of the alloy is reached within $55\,s$ by the surface when no oxidation is considered. If the oxide emissivity and chemical flux are considered, the fusion temperature of the alloy is reached within $63\,s$. An identical value is obtained when oxidation is modeled in depth and the conductivity is taken as $\lambda = 1\,\frac{W}{mk}$. Thus, the increase in emissivity outweighs the oxidation energy of reaction increasing the total time until melting, resulting in a net protective effect.

To simulate another flow condition, i.e., representative of another reentry point, the Stanton number was multiplied by a factor of 0.56. This factor was considered to avoid reaching the alloy fusion temperature, when oxidation is considered, and to be in the range of temperatures tested in the experimental growth measurements of [4], used as an input for the present model. Figure 13 shows the wall temperature history for the different testing cases. When oxidation is is disregarded, 'Metal' case, the material reaches the fusion temperature of Invar-36 in $93\,s$ in contrast to a maximum temperature of 1700 K (below the alloy fusion temperature) when oxidation is considered either as a surface or in-depth phenomena. This is attributed to the lower emissivity of the alloy when compared to the oxide (Fig. 7) that is translated in less energy being emitted through radiation to the environment as it is shown when comparing the radiation fluxes in Fig. 14. Moreover, the sample in-depth temperature is approximately constant during the heating phase.

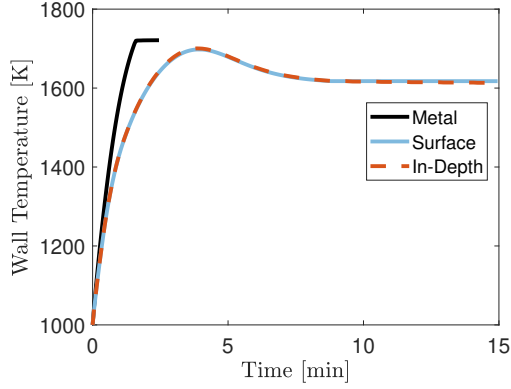Moreover, Fig. 13 shows no difference in wall temperature when in-depth modeling of oxidation is

Fig 13. Wall temperature history for $C_h = 0.012 \times 0.56$ for the different testing cases, for a sample thickness of $3\,\mathrm{cm}$ considering $\lambda = 1\,\frac{\mathrm{W}}{\mathrm{mk}}$
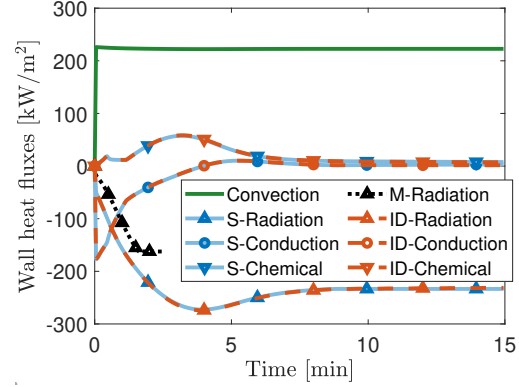

Fig 14. q^i in Eq. (2) for $C_h = 0.012 \times 0.56$ for no oxidation (M), oxidation modeled as a surface phenomena (S) or in depth (ID) for a sample thickness of $3\,\mathrm{cm}$ considering $\lambda = 1\,\frac{\mathrm{W}}{\mathrm{mk}}$

considered. Indeed the differences in volume specific heats, $\rho c_p|_{ox}$ and $\rho c_p|_{met}$, are small and extremely local. One could argue also that the difference in thermal diffusivity, $\alpha = \frac{\lambda}{\rho c_p}$, could be important since, as discussed previously, the conductivity is much lower on the oxide. However, this effect is not captured in this test case since the conductive heat flux tends to zero when high temperatures (associated with an high mass gain and oxide thickness) are achieved. From Fourier's law $q_w^{cond} = \lambda \frac{\partial T}{\partial x} \implies \partial T = q_w^{cond} \frac{\partial x}{\lambda}$ one sees that a decreasing conductive heat flux (due to the uniformization of the temperature field) competes with an increasing oxide thickness.

Figure. 13 shows also a temperature overshoot at around 4 minutes. Looking at the wall heat fluxes presented in Fig. 14 one observes a similar overshoot in the chemical heat flux. Indeed, at higher temperatures the oxide growth rate increases but retains its parabolic nature, i.e., very fast growth rates in the initial times and diminishing growth as thickness increases. This rapid mass increase is also translated in an higher chemical flux that increases the wall temperature. When the growth slows down, causing the chemical flux to decrease, radiation becomes the predominant term resulting in the cooling of the sample.

To evaluate the influence of sample thickness on the thermal behavior of the samples the three test cases are recomputed considering a domain with approximately 30 cm. The wall temperature time profile and the wall heat fluxes are shown in Fig. 15 and Fig. 16, respectively. One immediate conclusion is that, comparing different thicknesses, the time scale to reach similar temperatures is increased. Most importantly, the temperature overshoot present in Fig. 13 for the thin slab is not present for the thick domain. Analyzing the wall heat fluxes shown in Fig. 16 it is evident that the chemical heat flux no longer has an important contribution to the net heat flux. This is a consequence of the slow heating of the sample which does not promote abrupt mass gain. Moreover, no differences are noticed between in-depth and surface oxidation modeling. Indeed, as argued before, the conductive flux tendency to become zero as the temperature increases diminishes the effects captured with in-depth modeling.

5.1.2. Radiating posterior surface

In the present section, the posterior surface, previously considered adiabatic, is now taken as radiating to the environment as depicted in Fig. 12 together with the relevant fluxes schematic. The posterior surface is taken to be oxidized with an infinitesimal thick oxide layer so that emissivity is taken for the oxide but no chemical flux or in-depth modeling is considered. One important difference to the posterior adiabatic surface case is that when equilibrium is attained there is still a conductive flux through the front surface. For this reason, the effects of thermal diffusivity differences between oxide and alloy are more likely to be important when compared to the adiabatic surface case.
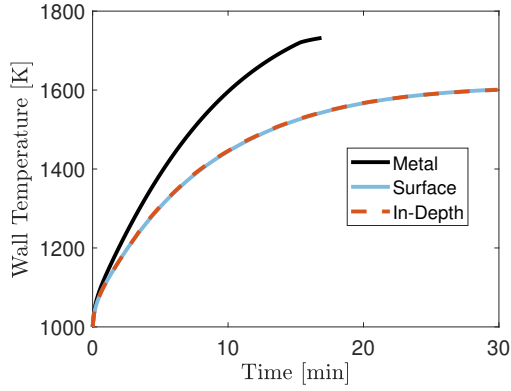
Fig 15. Wall temperature history for $C_h = 0.012 \times 0.56$ for the different testing cases, for a sample thickness of $30\,\mathrm{cm}$ considering $\lambda = 1\,\frac{\mathrm{W}}{\mathrm{mk}}$
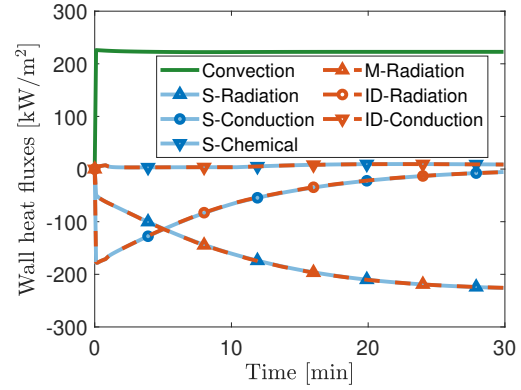

Fig 16. q^i in Eq. (2) for $C_h = 0.012 \times 0.56$ and for oxidation modeled in depth (ID) or as a surface phenomena (S), for a sample thickness of $30\,\mathrm{cm}$ considering $\lambda = 1\,\frac{\mathrm{W}}{\mathrm{mk}}$
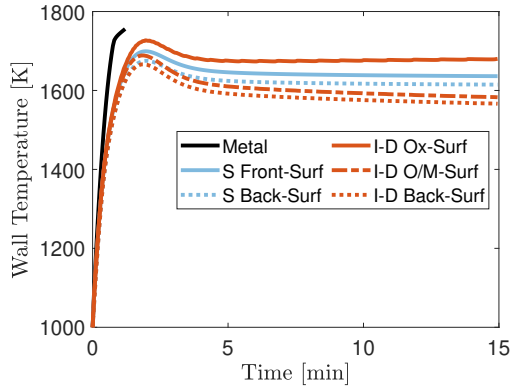

Fig 17. Wall temperature history for $C_h = 0.012 \times 1.17$ for the different testing cases, for a sample thickness of $3\,\mathrm{cm}$ and in-depth modeling considering $\lambda = 1\,\frac{\mathrm{W}}{\mathrm{mk}}$
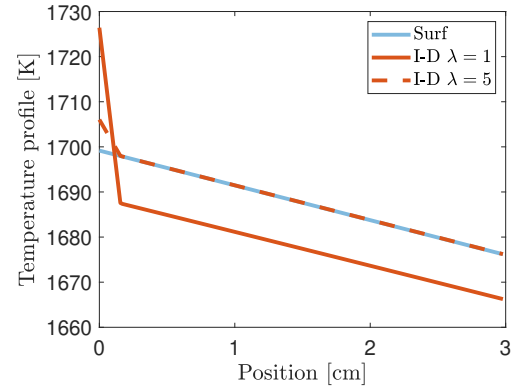
Fig 18. In depth temperature profiles for $C_h = 0.012 \times 1.17$ at $t = 120\,\mathrm{s}$ considering surface oxidation modeling or in-depth modeling with $\lambda = 1$ or $\lambda = 5\,\frac{\mathrm{W}}{\mathrm{mk}}$

Figure 17 shows the wall temperature history for the three testing conditions. Moreover, when applicable, it presents the temperatures of the posterior surface (Back-Surf), as well as the temperature in the oxide/metal interface (I-D O/M-Surf). For the present flow condition, $C_h = 0.012 \times 1.17$, the equilibrium temperature when oxidation is neglected is above the fusion temperature of Invar-36 and is reached in $48\,\mathrm{s}$. Moreover, Fig. 17 compares the temperature profile obtained with surface and in-depth oxidation modeling where an oxide conductivity $\lambda = 1\,\frac{\mathrm{W}}{\mathrm{mk}}$ is considered. The oxide wall temperature, when oxidation is modeled in-depth, is greater than when surface modeling is considered. However, evaluating the oxide/metal (O/M) interface temperature yields that this is lower for the in-depth model. Then, the oxide layer seems to have a protective effect for the interior alloy. Thus, for an higher heat flux flow condition, it is foreseeable that modeling oxidation as a surface phenomena one might predict alloy melting while when using in-depth modeling the interior alloy would not reach the fusion temperature.

To evaluate the influence of the oxide thermal diffusivity, two different values for conductivity were used to compute the in-depth temperature profile shows in Fig. 18. Two effects have to be considered when considering in-depth modeling effects: Firstly, the different thermal diffusivity will impose a different slope in the temperature profile. This is notorious on Fig. 18 where the slopes are different depending

Fig 19. Heat fluxes for $C_h = 0.012 \times 1.17$ for the different testing cases, for a sample thickness of 3 cm and in-depth modeling considering $\lambda = 1 \frac{\mathrm{W}}{\mathrm{mk}}$
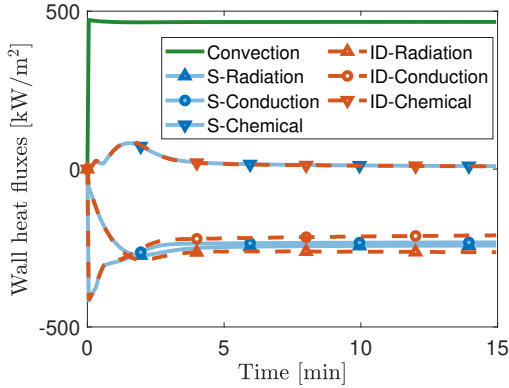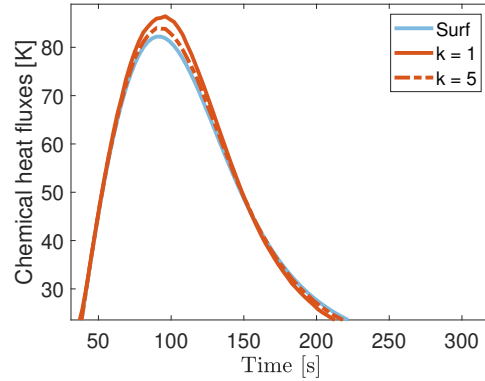

Fig 20. Chemical heat flux peak for $C_h = 0.012 \times 1.17$ for the different testing cases, for a sample thickness of 3 cm and in-depth modeling considering $\lambda = 1$ and $\lambda = 5 \frac{\mathrm{W}}{\mathrm{mk}}$

on the assumed conductivity. A decrease in oxide conductivity is protective since it increases the wall temperature on the oxide which has a higher fusion temperature, and will decrease the metal temperature, which has a lower fusion temperature. This effect will be greater the greater the difference in thermal conductivities between the alloy and the oxide. Hence it is important to have estimations of the oxide conductivity in this high temperature ranges. Secondly, the effect of changing the volumetric specific heat ρc_p, by oxidation of the material, has to be considered. For example, at $T = 1600\,\mathrm{K}$ the volumetric specific heat for the oxide is $\rho c_p|_{ox} = 4.81 \frac{\mathrm{J}}{\mathrm{m^3 K}}$ while for the alloy $\rho c_p|_{alloy} = 5.12 \frac{\mathrm{J}}{\mathrm{m^3 K}}$. Changing the material properties from alloy to oxide implies that less energy will be required to increase the temperature, justifying the increase in average wall temperature of the profiles obtained with the in-depth modeling when compared to the surface modeling results.

Figure 19 shows the wall heat fluxes history for surface and in-depth modeling using $\lambda = 1 \frac{\mathrm{W}}{\mathrm{mk}}$. Considering in-depth modeling translates into an increase in wall temperature (due to the slope imposed by the decreased thermal conductivity) that is translated into a higher heat lost by radiation. The chemical flux does not increase as significantly as radiation since the mass growth is based on the average oxide temperature instead of the oxide surface temperature.

The effect of thermal diffusivity change on the oxidation heat flux can be deduced from Fig. 20 where there seems to be a clear relation between the thermal diffusivity and the chemical heat flux. Indeed, the chemical heat flux is greater when the thermal diffusivity is lower. An argument for this can be made due to the dependency of the oxide growth on the average temperature of the oxide which is itself dependent on the temperature gradient. Figure 21 summarizes this argument and introduces further dependencies. Indeed, the increase in oxidation growth rate implies a heavier/thicker oxide, ∂x, which due to $\partial T = q_w^{cond} \frac{\partial x}{\lambda}$ implies a sharper temperature gradient. Furthermore, the chemical heat flux will also increase as stated by eq. (3) since more mass is being gained resulting in an higher average temperature and initiating the loop again.

Finally, Fig. 22 shows the temperature history for a thicker sample of 30 cm. The time scale is larger and more time is required to reach the alloy fusion temperature when no oxidation is considered. Regarding the chemical flux, the conclusions are similar as in the case of the adiabatic posterior surface. Due to the greater sample size heating is slower and no overshoot is noticed in the temperature history plot. However, one major difference, compared to the adiabatic case, is that the conductive flux is now not tending to zero due to the radiating surface. This is noticeable in the difference between the wall temperature and the oxide/metal interface temperature. Furthermore, the wall temperature obtained with the oxidation surface model is between the oxide surface and oxide/metal interface temperatures for the case of in-depth modeling. These temperatures are importantly different for the case where a conductivity $\lambda = 1 \frac{\mathrm{W}}{\mathrm{mk}}$ is
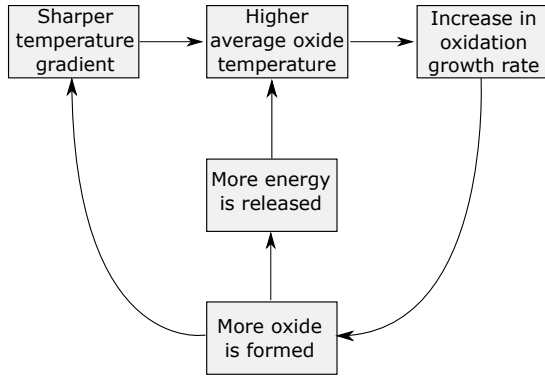
Fig 21. Schematic on the effects of lowering thermal diffusivity of the oxide.
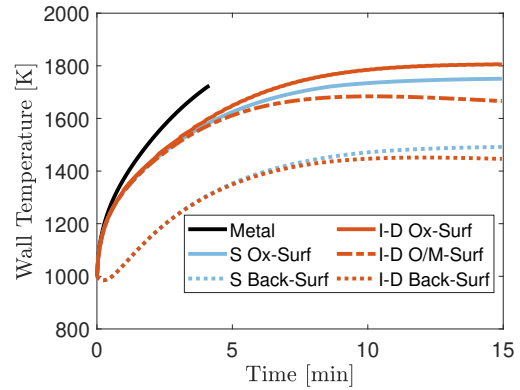

Fig 22. Wall temperature history for $C_h = 0.012 \times 1.17$ for the different testing cases, for a sample thickness of $30\,\mathrm{cm}$ and in-depth modeling considering $\lambda = 1\,\frac{\mathrm{W}}{\mathrm{mk}}$

considered. However, as conductivity/thermal diffusivity increases, this difference tends to be minor, reaching $\approx 30\,\mathrm{K}$ when a conductivity $\lambda = 5\,\frac{\mathrm{W}}{\mathrm{mk}}$ is considered.

6. Conclusions

The problem of space debris is currently a topic of intensive research, specifically, the development of physical models of debris demise for atmospheric reentry during which the formation of an oxide surface layer may arise. The present study presents numerical tools developed to evaluate oxidation of metallic materials. The oxide mass and thickness gains are numerically simulated in a 1-D finite difference framework which provides the basis for the implementation of a fully coupled mass-heat equation system that allows investigations of the thermal behavior of the reentering oxidizing material.

The influence of oxidation on the sample temperature history was studied with six test cases representing no-oxidation modeling and surface/in-depth oxidation modeling for adiabatic and radiating boundary conditions. CFD simulations were performed to retrieve the Stanton number and obtain explicitly the convective heat flux-wall temperature dependency. A novel approach was used to assess the growth of an oxide layer under heating conditions. Moreover, material properties for the alloy and oxide were taken both from thermodynamic libraries and the literature. The results were post-processed to evaluate the temperatures at specific points of the sample (front surface, oxide/metal interface, posterior surface) and the evolution of the relevant heat fluxes. The following specific conclusions can be drawn from the present work:

- Neglecting oxidation leads to an overestimation of the sample temperature as the increase in oxide emissivity far outweighs the chemical heat flux.

- When the posterior surface is adiabatic oxidation can be modeled as a surface phenomena due to the tendency of the conductive heat flux to be negligible after high temperatures are reached.

- When the posterior surface is radiating the conductive heat flux tends to a constant value. Thus, depending on the thermal diffusivity of the oxide, in-depth modeling can lead to important differences in thermal behavior when compared to surface modeling.

- Thin samples, which experience fast heating, present an overshoot in temperature due to the important chemical flux in the first stages of oxidation.

- Thick samples, which experience slow heating, tend smoothly to a constant behavior. In these cases, the oxidation chemical flux has a negligible effect.

References

[1] M Balat-Pichelin and P Omaly. Study of the atmospheric entry of metallic space debris–oxidation and emissivity evaluation to contribute to "design for demise". In *Proceedings of the 8th European Symposium on Aerothermodynamics for Space Vehicles*, 2015.

[2] Y. Prevereaud et al. Numerical and experimental study of the thermal degradation process during the atmospheric re-entry of a tial6v4 tank. *Acta Astronautica*, 122:258 – 286, 2016.

[3] T.J Nijdam, L.P.H Jeurgens, and W.G Sloof. Modelling the thermal oxidation of ternary alloys—compositional changes in the alloy and the development of oxide phases. *Acta Materialia*, 51(18):5295 – 5307, 2003.

[4] L. Barka et al. Oxidation and emissivity of invar 36 alloy in air plasma at high temperatures. *Journal of Alloys and Compounds*, 772:1003 – 1016, 2019.

[5] J Lis and PO Kellard. Measurements of the thermal conductivity of thin films of magnetite. *Journal of Physics D: Applied Physics*, 1(9):1117, 1968.

[6] O. Madelung and G.K. White. *Thermal Conductivity of Pure Metals and Alloys*. Springer-Verlag Berlin Heidelberg, 1991.

[7] P.F. Barbante. *Accurate and efficient modelling of high temperature nonequilibrium air flows*. PhD thesis, Université libre de brussels, May 2001.

[8] D. Bianchi. *Modeling of ablation phenomena in space applications*. PhD thesis, Universitá degli Studi di Roma, 06 2019.

[9] B. Sundman, B. Jansson, and J-O. Andersson. The thermo-calc databank system. *Calphad*, 9(2):153 – 190, 1985.

[10] Pedro Jorge. Development of oxidation models for space debris demise. Master's thesis, Von Karman Institute for Fluid Dynamics, 2019.

[11] I. Barin. *Thermochemical data of pure substances*. Federal Republic of Germany, 1989.

[12] O. Kubaschewski and B. E. Hopkins. *Oxidation of metals and alloys*. London:Butterworths, 1962.

[13] J. A. Nesbitts and R. W. Heckel. Interdiffusion in ni-rich, ni-cr-al alloys at 1100 and 1200 °c: Part ii. diffusion coefficients and predicted concentration profiles. *Metallurgical Transactions A*, 18(12):2075–2086, Dec 1987.

[14] Amir Faghri and Yuwen Zhang. *Transport phenomena in multiphase systems*. Elsevier, 2006.

[15] T.L. Bergman et al. *Fundamentals of heat and mass transfer*. John Wiley & Sons, 2011.

[16] A. Turchi et al. On the flight extrapolation of stagnation-point ablative material plasma wind tunnel tests. In *8th European Symposium on Aerothermodynamics for Space Vehicles*, pages 1–8, 2015.

[17] A. Atkinson. Transport processes during the growth of oxide films at elevated temperature. *Rev. Mod. Phys.*, 57:437–470, Apr 1985.

[18] M. Balat-Pichelin et al. Oxidation and emissivity of inconel 718 alloy as potential space debris during its atmospheric entry. *Materials Characterization*, 127:379 – 390, 2017.

[19] T Rooth, T Kelen, and J Arvesen. Deposition of impurities on heat transfer surfaces. the thermal conductivity of magnetite deposits. Technical Report STU–70-386/U317, Aktiebolaget Atomenergi, 1971.

[20] Y. Noda and K. Naito. The thermal conductivity and diffusivity of mnxfe3-xo4 from 200 to 700k. *Netsu Sokutei*, 5(1):11–18, 1978.

[21] Tomohiro Akiyama, Hiromichi Ohta, Reijiro Takahashi, Yoshio Waseda, and Jun-ichiro Yagi. Measurement and modeling of thermal conductivity for dense iron oxide and porous iron ore agglomerates in stepwise reduction. *ISIJ international*, 32(7):829–837, 1992.

[22] James B Scoggins and Thierry E Magin. Development of mutation++: Multicomponent thermodynamic and transport properties for ionized plasmas written in c++. In *11th AIAA/ASME joint thermophysics and heat transfer conference*, page 2966, 2014.